ACS NANO

www.acsnano.org

ARTICLE

Combining Microfluidic Assessment with Encoded Hydrogel Microparticle-Based Immunoassay for Anti-Interleukin Drug Repurposing of Pulmonary Fibrosis Therapy

Bolam Kim,[§] Hye Won Kim,[§] Jeong Yeon Kim, In Yeong Cho, Wookyoung Jang, Hyunsik Choi, and Ki Wan Bong*

Cite This: *ACS Nano* 2025, 19, 32361−32373

Read Online

ACCESS | Metrics & More | Article Recommendations | Supporting Information

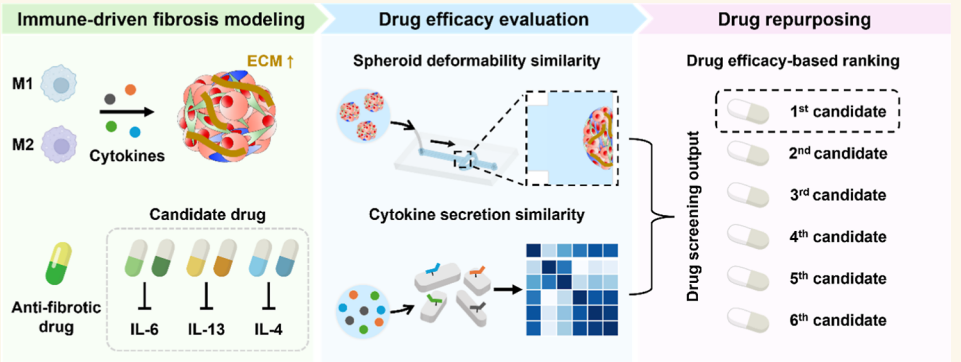

ABSTRACT: **Pulmonary fibrosis is a life-threatening disorder characterized by excessive extracellular matrix (ECM) deposition and progressive dysfunction. The disease progression is closely associated with increased ECM stiffness, which compromises normal tissue mechanics and leads to respiratory failure. Although its etiology is multifactorial, immune-mediated responses are central drivers of fibrotic remodeling through inflammatory cytokine release and aberrant tissue repair. Here, we present a microfluidic-integrated 3D immune spheroid platform for pulmonary fibrosis remodeling, featuring cytokine-secreting immune cells to induce fibrosis-like alterations in mechanical properties. This platform enables quantitative analysis of reversible changes in ECM stiffening and its modulation upon anti-interleukin drug administration using microfluidic mechanical assessment. Simultaneously, cytokine secretion profiles are obtained via multiplex immunoassays. Treatment with anti-interleukin agents elicited target-specific reductions in both spheroid stiffness and pro-inflammatory cytokine output. This integrated approach offers a screening-compatible preclinical tool to dissect immune-driven fibrotic dynamics and identify mechanically restorative antifibrotic therapies, highlighting the therapeutic repurposing potential of anti-interleukin drugs.**

KEYWORDS: *pulmonary fibrosis, mechanical properties, microfluidic, drug repurposing, fibrosis therapy*

INTRODUCTION

Pulmonary fibrosis is a progressive and often fatal lung disease characterized by excessive extracellular matrix (ECM) deposition, resulting in structural remodeling of lung tissue, increased stiffness, and gradual loss of pulmonary function.[1] These pathological changes ultimately lead to respiratory failure and death. Among various contributing factors, dysregulated immune signaling is increasingly recognized as a central driver of fibrotic remodeling. In particular, cytokines secreted by M1 macrophages (pro-inflammatory) and M2 macrophages (pro-healing) activate fibroblasts and promote their differentiation into ECM-producing myofibroblasts, thereby amplifying both

Received: May 14, 2025
Revised: August 25, 2025
Accepted: August 26, 2025
Published: September 4, 2025

https://doi.org/10.1021/acsnano.5c08033
ACS Nano 2025, 19, 32361−32373

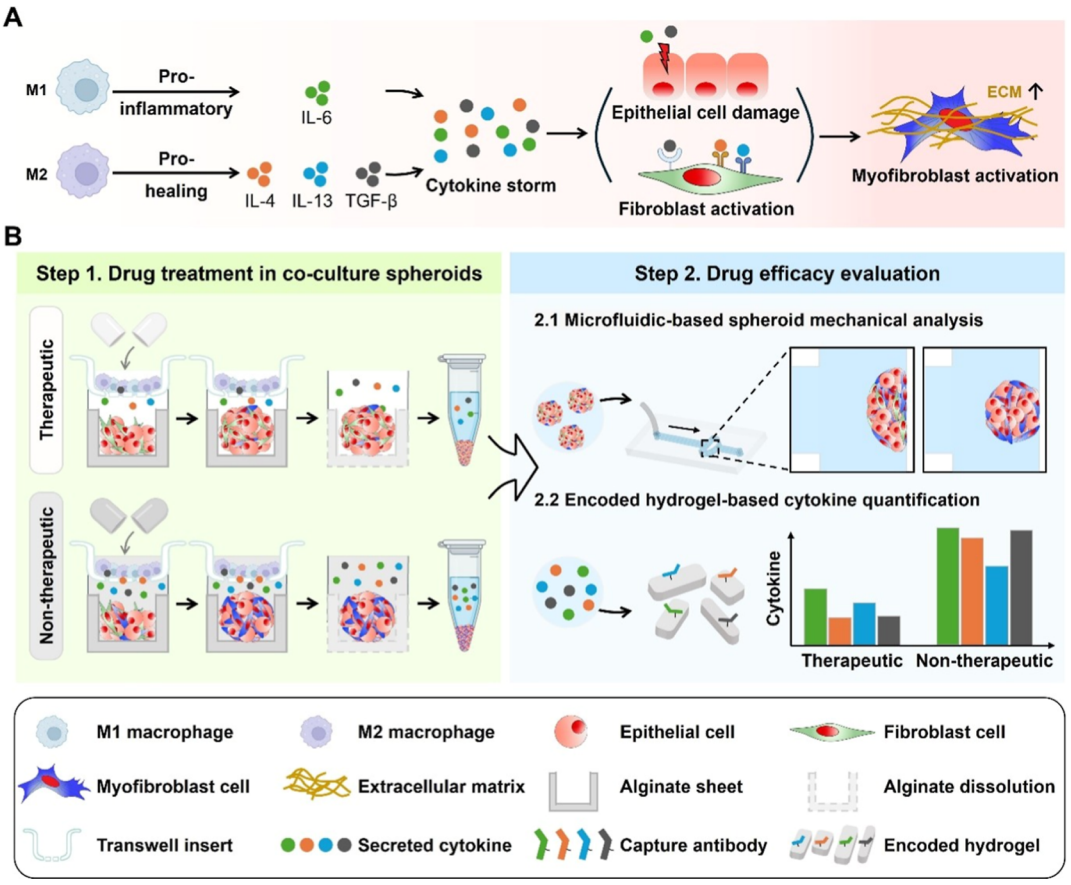

Figure 1. Schematic overview of microfluidic mechanical evaluation and multiplex cytokine profiling applied to anti-interleukin drug screening for pulmonary fibrosis. (A) Cytokine-mediated immune mechanisms contributing to pulmonary fibrosis. Pro-inflammatory (M1) and pro-healing (M2) macrophages secrete distinct cytokines that regulate fibroblast activation and ECM remodeling. Excessive cytokine release may trigger epithelial damage and fibroblast-to-myofibroblast transition, promoting fibrosis. (B) Workflow of anti-interleukin drug screening using a triple coculture spheroid model. Drug efficacy is assessed through microfluidic-based mechanical analysis of spheroids and encoded hydrogel based multiplex cytokine quantification.

ECM accumulation and mechanical alterations in the pulmonary microenvironment.[2−6]

Currently, nintedanib (NTD) and pirfenidone are the only antifibrotic drugs approved by Food and Drug Administration (FDA) for idiopathic pulmonary fibrosis (IPF), the most common form of pulmonary fibrosis. Nintedanib acts by broadly inhibiting fibrogenic signaling pathways such as transforming growth factor beta (TGF-β) and platelet-derived growth factor, while pirfenidone exerts antifibrotic, anti-inflammatory, and antioxidant effects through multiple, yet not fully defined, mechanisms.[7−10] Both drugs are known to slow the decline in lung function. However, their clinical efficacy remains limited, with variable responses across different fibrotic phenotypes, and their use is often restricted by adverse effects such as gastrointestinal and hepatic toxicity.[8,11] These limitations highlight the need for new therapeutic strategies with improved specificity, efficacy, and safety.

Recent advances in the immunopathogenesis of fibrosis underscore the potential of targeting cytokine-mediated immune signaling. In this context, drug repurposing, which is the use of existing drugs for new indications, has emerged as a promising strategy, offering advantages in safety, cost, and development time. Given the established roles of cytokines such as IL-6, IL-4, and IL-13 in immune-driven fibrosis, interleukin-targeted therapies represent attractive candidates for pulmonary fibrosis treatment. In particular, the anti-IL-13 monoclonal antibody tralokinumab (TRA) demonstrated the ability to attenuate fibrotic remodeling and preserve epithelial architecture in humanized mouse models.[12] However, in a phase 2 clinical trial involving patients with IPF, no significant improvement in lung function was observed, leading to early termination of the trial.[13] This outcome exemplifies the translational gap between preclinical efficacy and clinical utility, which often stems from fundamental limitations in conventional preclinical models that focus primarily on histological or molecular end points while neglecting biophysical tissue characteristics such as model stiffness. Among these biophysical features, tissue stiffening serves as an early and quantifiable indicator of fibrotic progression and exhibits strong correlation with both pulmonary function and clinical prognosis.[14] Recognizing the clinical relevance of tissue stiffening, biomechanical assessments are increasingly employed to improve the accuracy of disease progression evaluation. However, most existing studies rely on atomic force microscopy or microtweezer techniques that are constrained to single-cell resolution and are typically applied in matrix environments such as alginate or gelatin.[15−18] These conditions reflect matrix-driven mechanical changes but do not adequately capture the dynamic interactions between cells and between cells and the ECM. Microfluidic micropipette aspiration devices allow the advantage of directly measuring viscoelastic properties in intact spheroids.[19] However, their long acquisition times and inherently

https://doi.org/10.1021/acsnano.5c08033
ACS Nano 2025, 19, 32361−32373

low-throughput limit their scalability for high-throughput drug screening applications. Moreover, analyses based solely on changes in mechanical properties have limited capacity to reflect cytokine-level alterations that are closely associated with fibrotic remodeling, making it challenging to comprehensively assess drug efficacy. These limitations underscore the need for a combined platform capable of evaluating both mechanical and immunological responses to better identify therapeutically relevant candidates.

In this work, we propose an integrated evaluation strategy that combines mechanical analysis with cytokine secretion analysis of fibrotic remodeling. We previously developed a microfluidic platform for assessing mechanical properties of TGF-β induced pulmonary fibrosis spheroids, enabling quantitative stiffness analysis of disease progression.[20] However, this reductionist system lacked the cellular complexity and immune interactions observed in clinical fibrosis. To overcome this, we established a physiologically relevant 3D spheroid model comprising coculture lung fibroblast, endothelial cells, and cytokine secreting immune cells. This model better recapitulates the immune-fibrotic microenvironment and mimics clinically observed cytokine expression patterns. Using this platform, we evaluate four anti-interleukin agents as drug repurposing candidates and benchmarked their antifibrotic efficacy against nintedanib, an FDA-approved therapeutic.

Each candidate was administered to spheroids, and drug responses were assessed through (1) real-time mechanical profiling using our microfluidic deformation assay, and (2) multiplex cytokine analysis to capture immunomodulatory effects. Notably, among the four tested agents, tocilizumab (TCZ) exhibited mechanical and immunological response patterns that most closely resembled those of nintedanib. This observation aligns with previous clinical evidence showing that TCZ attenuates fibrotic progression in patients with systemic sclerosis-associated interstitial lung disease (SSc-ILD), in part by reducing circulating osteopontin levels, thereby further supporting the clinical relevance of our evaluation framework.[21] By integrating mechanical and immunological readouts within a spatiotemporally dynamics in vitro model, our study establishes a robust framework to more accurately evaluate immune-targeted antifibrotic therapies and enhance their translational relevance.

RESULTS AND DISCUSSION

Inflammatory Cytokine-Induced Fibrotic Remodeling. Monocytes are primarily circulating progenitor cells that migrate to sites of tissue injury in response to cytokines secreted at the damaged area and subsequently differentiate into macrophages. Once these monocytes reach the injured lung tissue, they differentiate into macrophages. Initially, M0 macrophages perform basic phagocytic functions and help maintain tissue homeostasis but have not yet acquired a polarized phenotype such as M1 or M2. In response to local microenvironmental cues, M0 macrophages can polarize into either the M1 or M2 phenotype. Specifically, polarization toward the M1 phenotype is primarily induced by pro-inflammatory stimuli such as interferon gamma, lipopolysaccharide, and GM CSF, whereas polarization toward the M2 phenotype is promoted by anti-inflammatory cytokines including IL-4, IL-13, IL-10, and M CSF. Accordingly, M1 macrophages secrete pro-inflammatory cytokines such as IL-6 and IL-12 to promote inflammatory responses, while M2 macrophages produce anti-inflammatory cytokines such as IL-4, IL-13, and TGF-β to support tissue repair.[6,22,23] However, excessive cytokine secretion may trigger a cytokine storm and imbalance, leading to epithelial cell damage and fibroblast activation, which in turn promotes the differentiation of fibroblasts into myofibroblasts.[24−26] This cascade increases ECM accumulation and alters the mechanical properties of the tissue, thereby accelerating the progression of fibrosis (Figure 1A).

The progression of pulmonary fibrosis is largely influenced by the inflammatory microenvironment, and effectively modeling this environment is essential to meet our research objectives. While previous studies have induced fibrosis using a model that relies solely on TGF β treatment, our study developed a triple coculture system that incorporates immune cells.[20] This system recapitulates an inflammatory cytokine milieu, thereby providing conditions that allow a more effective evaluation of the efficacy of anti-inflammatory drugs.

Based on the approach described above, we successfully differentiated monocytes into M0 macrophages using 100 nM Phorbol 12-myristate 13-acetate (PMA).[27] To generate a microenvironment conducive to further polarization, M0 macrophages were subsequently treated with 100 ng mL^{-1} LPS and 20 ng mL^{-1} IFN-γ for M1 induction or 20 ng mL^{-1} IL-4 and IL-13 for M2 induction.[28] The polarization status was confirmed by immunostaining for CD68 (M0 marker), CD80 (M1 marker), and CD206 (M2 marker) (Figures S1 and S2). After polarization, macrophages were thoroughly washed with fresh medium prior to harvesting and seeding onto transwell inserts for cytokine analysis. This washing step was necessary to remove residual IL-4 and IL-13 used during M2 induction, as these cytokines actively promote ECM remodeling in polarized M2 macrophages and could confound downstream assays. The selected analytes included the proinflammatory cytokine IL-6 and the pro-healing cytokines IL-4, IL-13, and TGF-β, which are closely associated with the progression of pulmonary fibrosis and are known to promote the differentiation of fibroblasts into myofibroblasts.[5] To enable high-sensitivity and multiplexed quantification of these four cytokines from small sample volumes, we employed an encoded particle-based detection system utilizing from PEG-based hydrogel microparticles with distinct aspect ratios.[29−33] Each particle type was functionalized with a specific antigen corresponding to IL-6, IL-4, IL-13, or TGF- β, allowing simultaneous detection within a single assay. The porous structure of the hydrogel facilitates efficient antigen−antibody interactions, enabling high-density target capture and enhanced signal amplification. Detailed information on the hydrogel particle morphology and the immobilized antigen is provided in Figure S3. This assay enabled the simultaneous detection of IL-6, IL-4, IL-13, and TGF-β in small volumes of culture supernatant, with detection limits of 2.18 pg/mL, 2.19 pg/mL, 6.01 pg/mL, and 8.76 pg/mL, respectively (Figure S4). These detection limits provide sufficient sensitivity to resolve subtype specific cytokine profiles, enabling reliable application in immune modulated fibrosis modeling and interleukin targeted drug evaluation.

Development and Characterization of Triple Coculture Fibrotic Spheroids. The conventional single-cytokine TGF-β-induced fibrosis model captures only a subset of the complex cellular interactions occurring in pulmonary fibrosis, particularly lacking the contribution of immune cell-derived cytokine signaling. To address this limitation, we first established a triple coculture spheroid model incorporating macrophages, lung epithelial cells and fibroblasts. As illustrated in Figure 2A, macrophages (M0, M1, and M2) were seeded in

https://doi.org/10.1021/acsnano.5c08033
ACS Nano 2025, 19, 32361−32373

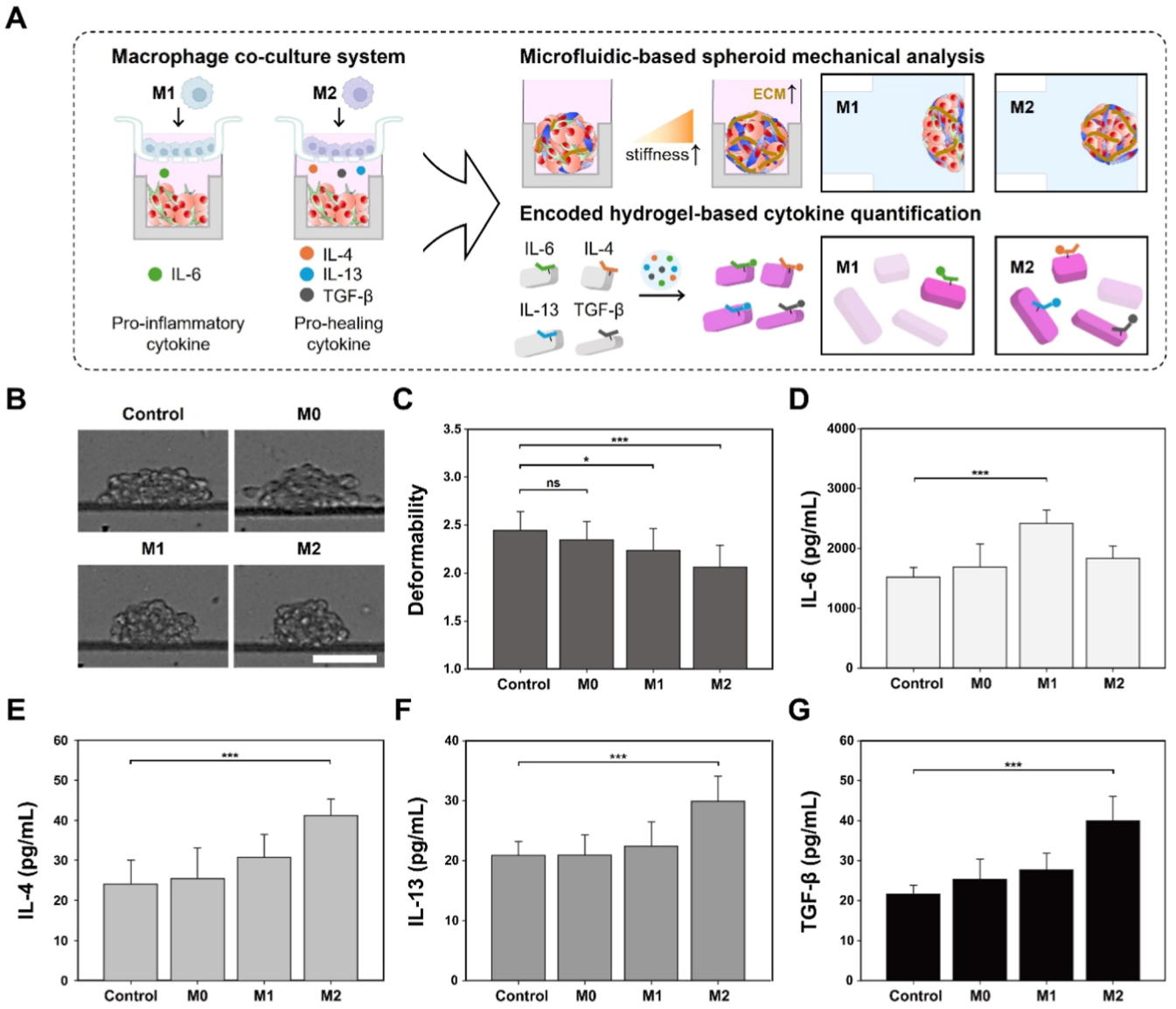

Figure 2. Macrophage subtype-specific pulmonary fibrosis modeling and functional characterization of lung spheroids. (A) Schematic illustration of the macrophage coculture system for modeling immune-driven pulmonary fibrosis, highlighting the polarization-dependent secretion of pro-inflammatory (IL-6) and pro-healing cytokines (IL-4, IL-13, TGF-β), as well as the downstream analysis of spheroid stiffness and cytokine profiling. (B) Representative images of spheroids in different coculture conditions. (C) Quantitative analysis of spheroid deformability under M0, M1, and M2 conditions ($n \geq 25$), revealing reduced deformability in M1 and M2 models. Cytokine quantification of (D) IL-6, (E) IL-4, (F) IL-13, and (G) TGF-β in culture supernatants after 48 h. Bar graphs show cytokines levels measured across different macrophage coculture conditions. M1 spheroids showed elevated IL-6 secretion, while M2 spheroids exhibited significantly increased IL-4, IL-13, and TGF-β levels compared to control. Scale bar indicates 100 μm. *$p < 0.05$, ***$p < 0.001$, n.s.: not significant.

the upper compartment of a transwell plate, while lung epithelial and fibroblast cells were cultured in the lower compartment to form spheroids.

Control spheroids were generated without immune cells under identical conditions. After 48 h of incubation, spheroids were gently harvested into PBS and directly subjected to microfluidic deformability analysis. Because cytokine analysis could not be performed concurrently with the deformability measurements, the collected supernatant was temporarily stored at −80°C and analyzed immediately upon completion of the mechanical assay. Validation experiments confirmed that short-term frozen storage (≤24 h) did not significantly affect cytokine concentrations, as shown in Figure S5. This dual-assessment approach enables simultaneous analysis of physical and biochemical remodeling. Providing a comprehensive framework for evaluating drug responses.

Spheroid deformability was assessed using a microfluidic deformation assay operated at a flow rate of 2.0 mL/min, which had been previously optimized based on spheroid size and microchannel dimensions to ensure accurate deformation measurement.[20] The design of the microfluidic device and the methodology for calculating spheroid deformability based on flow-induced deformation are illustrated in Figure S6. Spheroid deformability was quantified by calculating the ratio of the major axis (Xd, perpendicular to flow) to the minor axis (Yd, parallel to flow). Prior to mechanical assessment, the uniformity of spheroid size was confirmed to minimize variability. As shown in Figure S7, uniformly sized spheroids were successfully generated, with no detectable size differences between immune

https://doi.org/10.1021/acsnano.5c08033
ACS Nano 2025, 19, 32361−32373

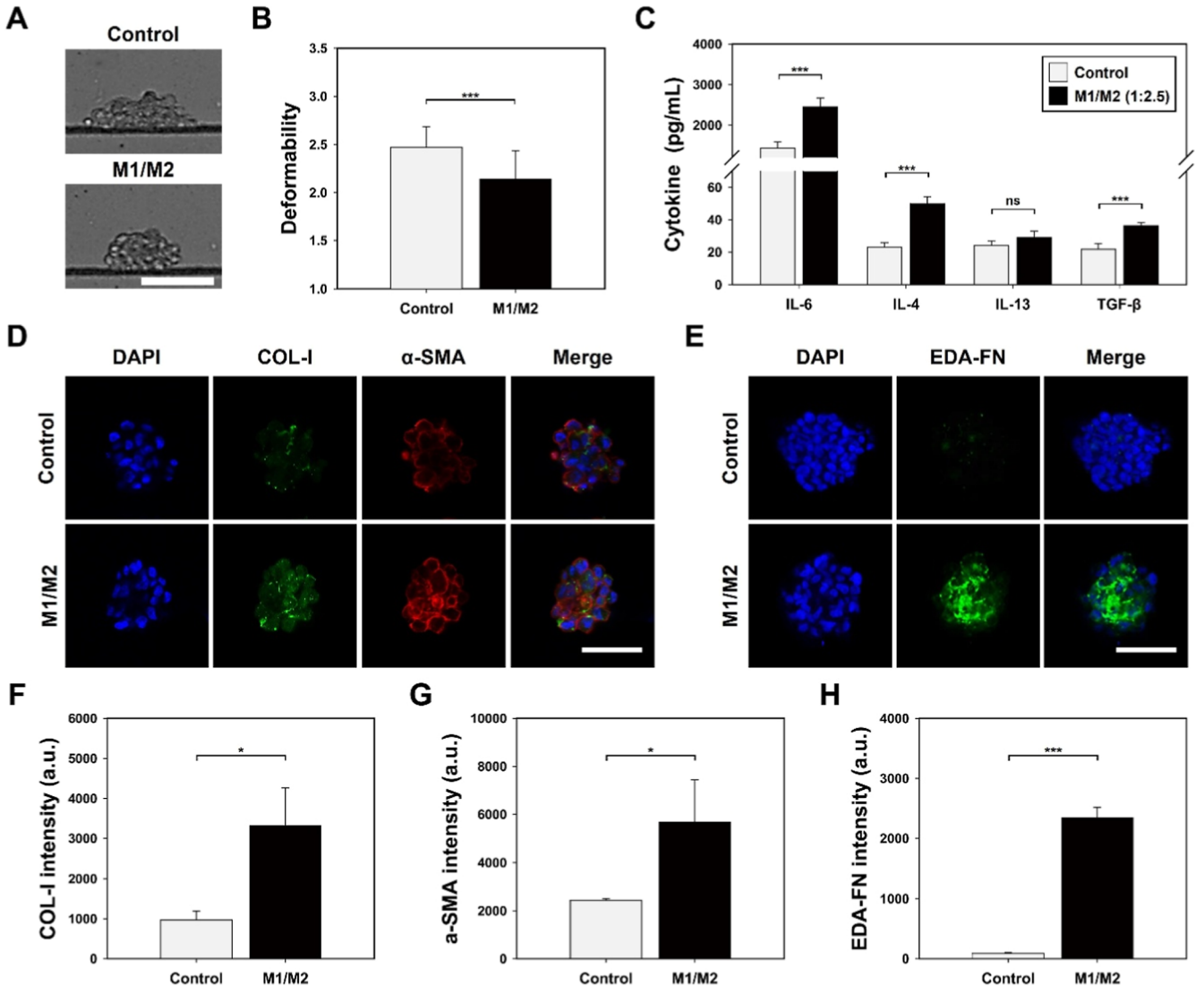

Figure 3. Characterization of pulmonary fibrosis spheroid model under clinically relevant macrophage polarization conditions. (A) Representative images of spheroids subjected to microfluidic deformation analysis, comparing control and M1/M2 (1:2.5) coculture conditions. (B) Quantification of spheroid deformability. Deformability was calculated as the ratio of the major axis (Xd) to the minor axis (Yd) under flow. A significant decrease of 10.2% was observed compared to control ($n \geq 25$). (C) Cytokine concentrations of IL-4, IL-6, IL-13, and TGF-β in the supernatant of coculture spheroids (M1/M2 = 1:2.5), quantified using a hydrogel particle-based multiplex assay. (D) Confocal fluorescence images showing the expression of fibrosis-associated markers collagen-I, α-SMA, and (E) EDA-FN in spheroids under control and M1/M2 (1:2.5) coculture conditions. Quantitative analysis of fluorescence intensity for (F) collagen-I, (G) α-SMA, and (H) EDA-FN, normalized to the DAPI-stained nuclear area of each spheroid. Scale bars indicate 100 μm. *p < 0.05, **p < 0.01, ***p < 0.001, n.s.: not significant.

cell-containing and control spheroids. To verify the reproducibility of our previous work and to establish a reference benchmark that clearly separates the normal and disease categories, we reproduced the previously reported control-fibrosis-therapy triad (Figure S8): (i) normal (control) pulmonary spheroids, (ii) TGF-β-induced fibrotic spheroids, and (iii) fibrotic spheroids treated with the clinically validated antifibrotic agent NTD. Mean deformability (±SD) values were 2.45 ± 0.23 (control), 2.23 ± 0.19 (TGF-β), and 2.55 ± 0.25 (TGF-β + NTD), demonstrating a clear mechanical shift with fibrosis and a drug-induced return toward the normal range. These results establish a semiquantitative reference line for distinguishing normal from fibrotic states within our assay and reconfirm the validity of deformability-based efficacy evaluation, thereby strengthening the basis for antifibrotic drug screening.

Mechanical analysis showed macrophage polarization-dependent modulation of spheroid stiffness (Figure 2B,C; Movies S1, S2, S3, and S4). In the M1 macrophage coculture model, deformability decreased by 6.2% (from 2.41 ± 0.22 to 2.26 ± 0.20), whereas in the M2 macrophage coculture model, deformability decreased by 13.7% (from 2.41 ± 0.22 to 2.08 ± 0.20). Notably, M2 macrophages induced a 7.2% greater reduction in deformability compared to the TGF-β treated model (Figure S9), indicating a synergistic role of immune-derived cytokines in promoting fibrotic remodeling.

To further investigate cytokine secretion, levels of IL-6, IL-4, IL-13, and TGF-β were quantified using an encoded hydrogel microparticle-based multiplex immunoassay. As shown in Figure 2D, IL-6 levels were elevated 1.61-fold under the M1 condition relative to control, consistent with the pro-inflammatory nature

https://doi.org/10.1021/acsnano.5c08033
ACS Nano 2025, 19, 32361−32373

of M1 macrophages.[34,35] In contrast, only M2 coculture resulted in significant increases in IL-4 (1.58-fold), IL-13 (1.42-fold), and TGF-β (1.89-fold) (Figures 2E−G). These results confirm that M2 macrophages actively regulate the fibrotic cytokine microenvironment, which correlates with increased spheroid stiffness. Together, the mechanical remodeling and multiplex cytokine profiling indicate that pulmonary fibrosis progression is governed by a complex network of immune cell-derived cytokines rather than by TGF-β alone. This highlights the importance of incorporating immune complexity into physiologically relevant in vitro fibrosis models for mechanistic studies and therapeutic screening.

Optimization of Macrophage Polarization Ratio for Fibrosis Modeling. As previously discussed, the mechanical properties and cytokine milieu of spheroids depend on macrophage subtype. To more precisely recapitulate the pathological features of pulmonary fibrosis, we established a macrophage polarization ratio reflecting clinically relevant conditions. According to literature reports, IL-6 and IL-4 levels in fibrotic lung tissues increase by 1.50−2.26 fold and 2.00−3.49 fold, respectively (Table S1). Additionally, Immunohistochemical analyses have demonstrated that M2 macrophages are over 2-fold more abundant than M1 macrophages in lung tissues of patients with pulmonary fibrosis, indicating a predominance of M2 polarization in the fibrotic microenvironment.[3,6] To reflect these clinical cytokine shifts within the in vitro model, we first profiled cytokine secretion as a function of macrophage subtype and cell number using the encoded hydrogel microparticle-based multiplex immunoassay described previously (Figure S10). Based on these reference data, the relative proportions of M1 and M2 macrophage were computationally adjusted so that the resulting IL-6 and IL-4 secretion levels from the triple coculture system would align with the clinical ranges reported in patient samples. This approach led to the selection of an M1/M2 ratio of 1:2.5, which successfully reproduced the targeted cytokine profile (Table S2). Using this optimized ratio, triple coculture spheroids were generated to model fibrotic conditions. To determine whether this configuration recapitulates key immunopathological features of pulmonary fibrosis, we systematically evaluated spheroid mechanical properties, cytokine secretion profiles, and conventional fibrotic marker expression.

The mechanical properties of spheroids were first assessed using our previously described microfluidic deformation assay (Figure 3A,B). When macrophages were cocultured at the clinically inspired ratio of M1:M2 − 1:2.5, spheroid deformability decreased by 10.2% compared to the control (from 2.45 ± 0.23 to 2.20 ± 0.23, Movie S5) and was also lower than in M2-only cultures, consistent with the convergence of sustained pro-inflammatory (IL-1β/TNF-α) and pro-fibrotic (IL-4/IL-13/TGF-β) signaling that promotes fibroblast activation, myofibroblast differentiation, and ECM accumulation. This configuration better emulates clinically relevant immune-fibrotic crosstalk than single-factor models (e.g., TGF-β or bleomycin). Furthermore, treatment of these spheroids with a clinically approved antifibrotic agent partially restored their deformability, confirming that the observed mechanical stiffening reflects fibrosis-associated pathology (Figure S11). This pharmacological reversibility further supports the validity of the coculture spheroid system as a translationally relevant model of immune-driven pulmonary fibrosis.

We next analyzed the cytokine environment by quantifying IL-6, IL-4, IL-13, and TGF-β levels in the supernatant collected from the coculture model (Figure 3C). The concentration of IL-6 and IL-4 levels increased by 1.71-fold and 2.17-fold, respectively, closely aligning with trends reported in IPF patient data.[36,37] Similarly, the levels of TGF-β was significantly elevated, supporting its role in the process of tissue fibrosis. However, IL-13 levels remained statistically unchanged compared to the control (24.12 pg/mL), and a similar level was observed in the M1/M2 coculture condition (28 pg/mL, Figure 2F). This lack of upregulation may be attributed to the antagonistic influence of M1 macrophages, which are known to suppress IL-13 activity through cytokine-mediated inhibition of the STAT6 pathway and increased expression of decoy receptors such as IL-13Rα2.[38] Taken together, these results suggest that in coculture environments, M1 derived pro-inflammatory signals can attenuate M2 derived IL-13 production, highlighting the limitations of interpreting immune crosstalk based solely on individual cytokines levels. This phenomenon may also explain why IL-13 is often underrepresented in patient cytokine profiles despite its known profibrotic roles.

Finally, we analyzed the expression of traditional fibrotic markers, collagen-I, α-SMA, and extra domain A-fibronectin (EDA-fibronectin) via immunofluorescence. To quantitatively compare marker expression across spheroids, the fluorescence intensities of collagen-I, α-SMA, and EDA-fibronectin were normalized to the DAPI stained nuclear area of each spheroid, enabling standardized comparison based on cell density (Figure 3D,E). Due to spectral overlap between collagen-I and EDA-fibronectin, which were both labeled with FITC, these markers were visualized in separate immunofluorescence assays. Therefore, collagen-I was costained with α-SMA, and EDA-fibronectin was examined independently. To confirm that fluorophore interference did not affect signal quantification, α-SMA was additionally costained with EDA-fibronectin. The fluorescence intensity of α-SMA remained consistent between both staining combinations, validating that no measurable interference occurred during multiplexed imaging (Figure S12). Under the M1/M2 coculture condition, the expression of collagen-I, α-SMA, and EDA-fibronectin increased by 243.67, 133.14, and 2489.62%, respectively, compared to the control, reflecting robust ECM remodeling and myofibroblast activation, (Figure 3F−H). These pronounced increase in fibrotic markers demonstrate the ability of our coculture model to recapitulate hallmark features of tissue remodeling. Notably, such fibrotic remodeling arises not from a single signaling axis but likely results from the integrated effects of immune cell-derived cytokine interactions. Taken together, these results support the notion that pulmonary fibrosis is governed by complex immune-derived signaling network. Our macrophage integrated coculture spheroid system successfully captures this pathophysiological complexity, offering a robust in vitro platform for both mechanistic studies and antifibrotic drug repurposing.

Evaluation of Anti-Interleukin Drugs for Antifibrotic Efficacy. To identify key cytokine targets for antifibrotic drug repurposing, we focused on IL-6, IL-4, IL-13, and TGF-β based on their established roles in the pathogenesis of pulmonary fibrosis. IL-6 is a pleiotropic proinflammatory cytokine that enhances inflammatory responses and has been shown to indirectly promote ECM.[39,40] This effect is mediated through its cooperation with colony-stimulating factor-I (CSF-I) to induce the expression of secreted phosphoprotein-1(SPP-I) in lung macrophages. SPP-I promotes epithelial to mesenchymal transition and fibroblast activation by enhancing TGF-β signaling, thereby facilitating fibrotic remodeling.[21] In contrast, IL-4 and IL-13, although typically associated with tissue repair,

https://doi.org/10.1021/acsnano.5c08033
ACS Nano 2025, 19, 32361−32373

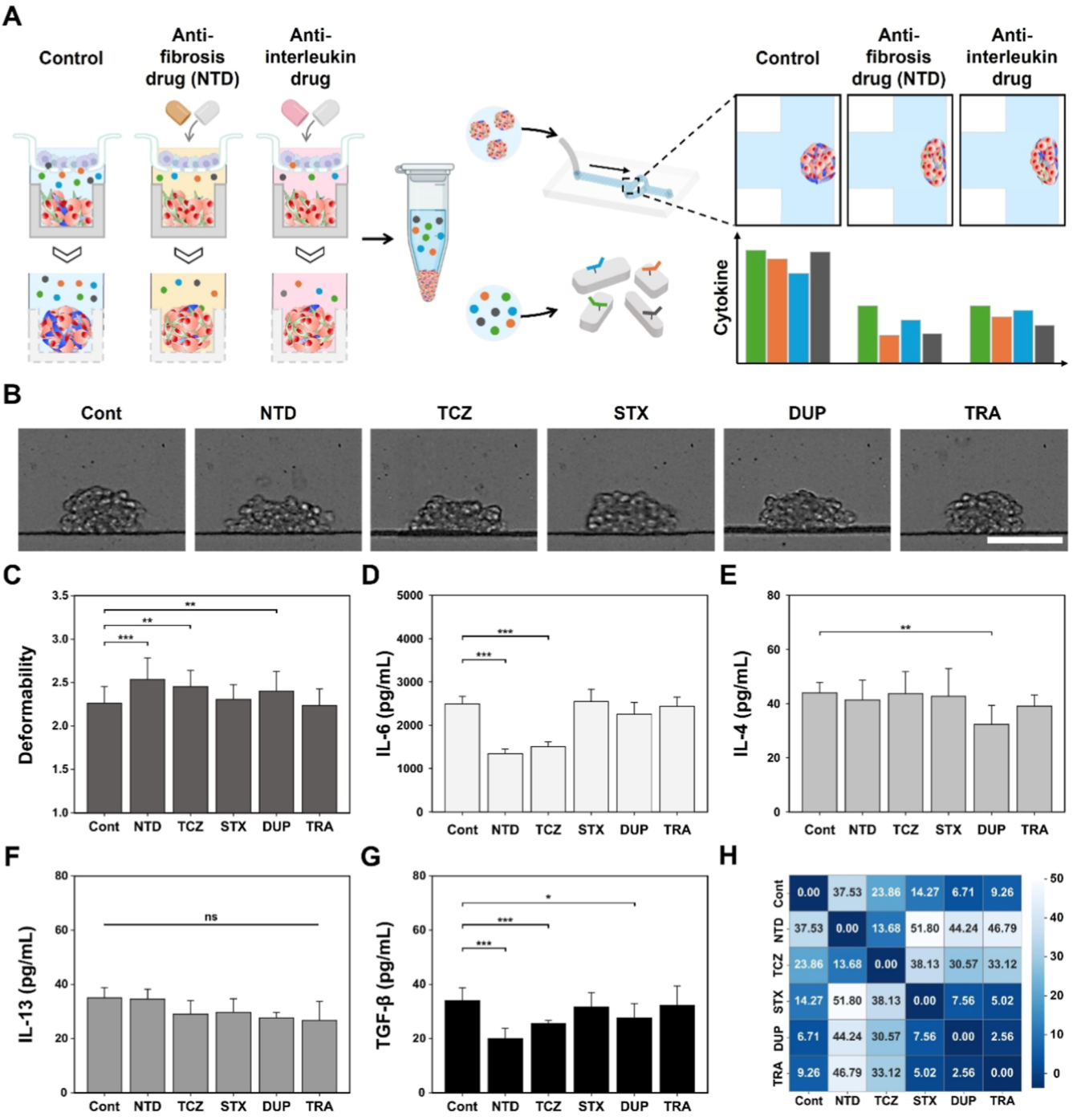

Figure 4. Evaluation of anti-interleukin drug efficacy on fibrosis-induced spheroids. (A) Schematic representation of the drug-screening workflow evaluating anti-interleukin drug efficacy through spheroid mechanical analysis and multiplex cytokine quantification. (B) Representative images of spheroids subjected to microfluidic deformation analysis, comparing untreated control, antifibrotic drug NTD, and anti-interleukin drugs TCZ, STX, DUP, and TRA. (C) Quantification of spheroid deformability showing an increase of 13.02% (NTD), 7.70% (TCZ), 2.34% (STX), 7.69% (DUP), and 0.88% (TRA) compared to control ($n \geq 25$). (D−G) Cytokine concentrations measured in culture supernatants following drug treatments: (D) IL-6, (E) IL-4, (F) IL-13, and (G) TGF-β. (H) Drug similarity heatmap based on IL-6, IL-4, and TGF-β levels normalized to IL-13. Scale bar indicates 100 μm. *$p < 0.05$, **$p < 0.01$, ***$p < 0.001$, n.s.: not significant.

have been shown to exacerbate fibrosis in chronic disease contexts. These cytokines drive the polarization of macrophages toward the M2 phenotype, which is known to upregulate TGF-β secretion and stimulate collagen synthesis. Genetic knockout studies targeting IL-4 receptor-α or IL-13 have demonstrated a marked reduction in fibrosis severity, further supporting their roles in fibrogenesis. Based on these findings, we selected IL-6, IL-4, IL-13, and TGF-β as key targets for antifibrotic drug evaluation.

In this study, we used the FDA-approved pulmonary fibrosis drug nintedanib (NTD) as a positive control and treated pulmonary fibrosis model spheroids with four candidate cytokine inhibitors closely associated with the development of pulmonary fibrosis. Drugs that target IL-6 include TCZ and

https://doi.org/10.1021/acsnano.5c08033
ACS Nano 2025, 19, 32361−32373

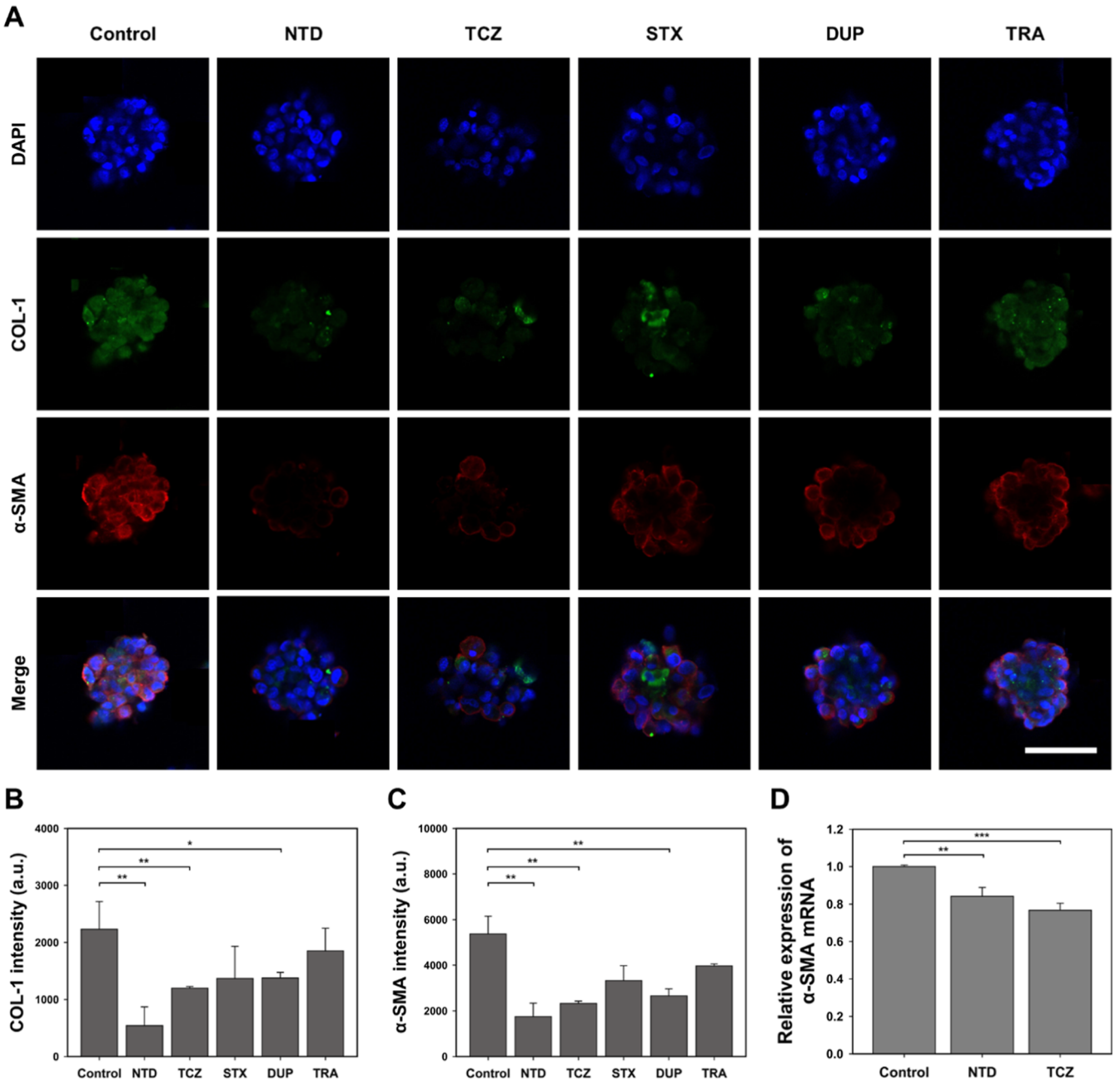

Figure 5. Expression of fibrosis-associated markers in drug-treated spheroids. (A) Confocal fluorescence images showing the expression of collagen-1 and α-SMA in spheroids treated with NTD, TCZ, STX, DUP, and TRA. (B) Quantitative analysis of fluorescence intensity for collagen-1, normalized to the DAPI-stained nuclear area of each spheroid. Expression significantly decreased by 72.63% (NTD), 50.28% (TCZ), and 43.39% (DUP) compared to untreated control ($n = 3$). (C) Quantitative analysis of fluorescence intensity for α-SMA, normalized to the nuclear area. Expression significantly decreased by 64.34% (NTD), 58.73% (TCZ), and 53.43% (DUP) compared to untreated control ($n = 3$). (D) Relative mRNA expression level of α-SMA in spheroids treated with NTD and TCZ, normalized to glyceraldehyde 3-phosphate dehydrogenase (GAPDH) expression ($n = 3$). Scale bars indicate 100 μm. *$p < 0.05$, **$p < 0.01$, ***$p < 0.001$.

siltuximab (STX). TCZ is a humanized antibody developed by grafting the complementarity determining regions of a mouse antihuman IL-6 receptor antibody onto human IgG1 kappa. It binds to the IL-6 binding site of the human IL-6 receptor and competitively inhibits IL-6 signal transduction. In contrast, STX binds directly to IL-6 and prevents its interaction with the IL-6 receptor (Figure S13). Meanwhile, drugs related to pro-healing cytokines that promote tissue repair such as IL-4 and IL-13 include dupilumab (DUP) and TRA. DUP binds to the common IL-4 receptor alpha chain present in both the IL-4 and IL-13 receptors and blocks the effects of both cytokines, whereas TRA targets IL-13 to inhibit its signal transduction. To investigate the potential of drug repurposing, we administered interleukin targeting inhibitors corresponding to each cytokine in a macrophage integrated spheroid model and assessed both the mechanical properties of the spheroids and cytokine secretion profiles (Figure 4A). To exclude drug-induced cytotoxicity as a confounder, we quantified viability at the same end point. No significant differences in viability were observed between the untreated fibrotic control and any drug-treated group ($p > 0.05$), indicating that the observed changes in

https://doi.org/10.1021/acsnano.5c08033
ACS Nano 2025, 19, 32361−32373

deformability are not attributable to loss of viable mass (Figure S14).

The mechanical properties of spheroids were evaluated using the microfluidic system (Figure 4B,C; Movies S6, S7, S8, S9, and S10). Spheroids treated with TCZ exhibited the most similar mechanical characteristics to those treated with NTD, with a nonsignificant difference in deformability (p-value = 0.098). Additionally, the DUP treated group demonstrated a statistically significant difference in deformability compared to the fibrotic control group generated by M1/M2 coculture. In contrast, the mechanical stiffness observed in fibrotic spheroids was maintained following STX and TRA treatment, as evidenced by both deformation values and morphological imaging.

Cytokine levels under each drug treatment condition were quantified using a hydrogel-based multiplexed assay system. As shown in Figure 4D, IL-6 secretion in the NTD treated group decreased by up to 46.8% compared to the fibrotic control. This observation is consistent with previous reports demonstrating that NTD suppresses the production of proinflammatory cytokines such as IL-6.[8] In contrast, the IL-6 targeting drugs TCZ and STX led to reductions of 40.4 and 7.03% respectively. Notably, these two drugs differ substantially in their mechanisms of action. TCZ binds competitively to the IL-6 receptor, thereby inhibiting receptor engagement and downstream IL-6/STAT3 signaling. This inhibition may attenuate proinflammatory gene expression and has been associated with reduced IL-6 production in certain inflammatory contexts, possibly through feedback regulation of cytokine expression. In contrast, STX directly binds to soluble IL-6 and neutralizes its activity by preventing interaction with the IL-6 receptor complex. However, this neutralization does not suppress IL-6 biosynthesis. Instead, STX forms stable IL-6 antibody complexes that may persist in the medium, potentially leading to unchanged or even elevated total IL-6 levels as measured by immunoassays, due to the accumulation of bound IL-6.[40,41] Taken together, these mechanistic differences explain why IL-6 levels in the STX treated group did not decrease significantly, unlike those in the TCZ treated group. These results suggest that TCZ, similar to NTD, may reduce the production of proinflammatory cytokines through alternative signal transduction pathways.[42]

In addition, according to Figure 4E, only DUP treatment resulted in a statistically reduction in IL-4 levels, with a p-value of 0.005. TGF β, which activates fibroblast cells and induces ECM accumulation, was significantly reduced only in the NTD, TCZ, and DUP groups (Figure 4G).

Notably, IL-13 secretion did not differ significantly across all conditions, including both the control and drug treated group (Figure 4F). As described above, this may be attributed to the antagonistic effect of M1 macrophages on IL-13 secretion from M2 macrophages. Based on these findings, IL-6, IL-4, and TGF-β levels were normalized to IL-13 level to assess relative cytokine balance under each drug treatment. To compare immunomodulatory effects among treatment groups, we performed hierarchical clustering on the normalized cytokine ratios (IL-6/IL-13, IL-4/IL-13, and TGF-β/IL-13) and visualized the results as a heatmap (Figure 4H). Similarity between cytokine ratios was quantified using Euclidean distance, where lower values indicate greater similarity. This clustering approach allowed us to identify drugs that exert comparable effects on cytokine regulation. Notably, NTD and TCZ exhibited closely aligned cytokine ratios and clustered together, consistent with their similar mechanical outcomes. This analytical strategy provides a multidimensional perspective on drug responses and facilitates the evaluation of functional similarity among candidate antifibrotic compounds.

These experimental findings are consistent with reported clinical results. Specifically, a clinical trial demonstrated that weekly subcutaneous administration of 162 mg of TCZ for 48 weeks helped maintain lung function in patients with early systemic sclerosis-associated interstitial lung disease (SSc-ILD).[43] In contrast, TRA, an IL-13 targeting drug, was reported to have failed in clinical trials for IPF due to insufficient efficacy, ultimately resulting in study termination.[13] Notably, in our study, the TCZ treated group exhibited a clear improvement in spheroid deformability and a significant reduction in IL-6 secretion compared to the fibrotic control, whereas the TRA treated group showed no appreciable changes in either mechanical stiffness or cytokine profile. This strong concordance between clinical efficacy and in vitro results highlights the reliability of our macrophage integrated 3D spheroid platform as a predictive tool for antifibrotic drug screening. By capturing both biomechanical remodeling and immunological modulation, the system offers a translationally relevant system for prioritizing drug candidates for clinical development.

Finally, we evaluated the expression of classical fibrotic markers, including collagen-I, α-SMA, and fibronectin-EDA, using immunofluorescence analysis (Figures 5 and S15). In line with the results from mechanical property- and cytokine-based evaluations, TCZ-targeted groups showed marked reductions in fibrotic protein expression ($p < 0.01$).

To further verify the molecular effects of TCZ, which was identified in our earlier analyses as a promising antifibrotic candidate, we performed quantitative real-time PCR (qPCR) to assess the gene expression of α-SMA, a representative myofibroblast marker (Figure 5D). TCZ treatment significantly reduced α-SMA gene expression compared with fibrotic model spheroids, exhibiting a suppression pattern similar to that observed with NTD.

Given the high cost and labor-intensive nature of individual immunostaining for fibrotic markers, our approach, which combines microfluidic mechanical assessment with encoded hydrogel microparticle-based multiplex cytokine profiling, offers a rapid, quantitative, and scalable platform for high-throughput antifibrotic drug screening-supporting both novel candidate discovery and drug repurposing efforts.

In summary, this integrated analysis supports the crucial roles of IL-6 and TGF-β in the progression of pulmonary fibrosis. The similarity in cytokine distribution and mechanical properties between the NTD and TCZ treated groups suggests that effectively inhibiting these pathways is key to treatment. Our findings indicate that interleukin-targeting drugs can rebalance cytokine signaling and improve both chemical and mechanical tissue properties, providing promising foundational data for drug repurposing strategies in pulmonary fibrosis therapy.

CONCLUSIONS

In this study, we developed a macrophage integrated 3D coculture spheroid model that quantitatively recapitulates key pathophysiological features of pulmonary fibrosis and provides an integrated platform for antifibrotic drug assessment. By implementing an M1/M2 polarization ratio of 1:2.5 based on clinical data, our model effectively simulated a cytokine milieu characteristic of fibrotic lung tissues.

Using a microfluidic collision-based system, we quantified mechanical changes in spheroids and demonstrated that cytokines secreted by polarized immune cells modulate ECM

https://doi.org/10.1021/acsnano.5c08033
ACS Nano 2025, 19, 32361−32373

stiffness. This mechanical response serves as a reliable physical readout for fibrosis progression. Cytokine quantification further revealed upregulation of IL-6, IL-4, and TGF-β under the coculture condition, while IL-13 levels remained statistically unchanged compared to the control despite its high expression in M2 only cultures. This observation suggests antagonistic interactions from M1 macrophages and underscores the complexity of immune-mediated regulation that cannot be captured by analyzing single cytokines in isolation.

To validate the fibrotic phenotype, we assessed the expression of conventional fibrosis markers, including collagen-I, α-SMA, and EDA-fibronectin. These markers, which commonly used in traditional fibrosis studies, served as benchmarks for comparison with our quantitative platform and confirmed ECM remodeling and myofibroblast activation within the spheroids. Furthermore, we performed quantitative real-time PCR analysis for α-SMA to verify the gene-level regulation of myofibroblast activation, further supporting the immunofluorescence findings.

Finally, we employed a dual-assessment strategy, combining mechanical property analysis with cytokine profiling, to evaluate the antifibrotic efficacy of anti-interleukin drug candidates. TCZ, in particular, demonstrated biomechanical responses comparable to those of nintedanib. It also exhibited similar cytokine balance patterns when normalized to IL-13. This suggests a promising repurposing potential for interleukin-targeting drugs in fibrosis therapy.

Although the present study focused on single-agent screening, the integrated platform could, in principle, be extended to explore combinatorial cytokine blockade (e.g., IL-6 and IL-4/IL-13). Given context-dependent efficacy signals and the potential for additive immunosuppression, such exploration should be hypothesis-driven and accompanied by appropriate safety safeguards. Accordingly, combination use remains a hypothesis-generating direction for future studies.

Overall, our coculture spheroid model offers a physiologically relevant and analytically robust in vitro platform that captures the immune mediated complexity of pulmonary fibrosis. It enables simultaneous evaluation of biomechanical and inflammatory results, thereby facilitating precise mechanistic studies and preclinical screening of antifibrotic therapeutics.

MATERIALS AND METHODS

Materials. Human fetal lung fibroblast cell line (MRC-5), human lung epidermoid carcinoma cell line (Calu-1), and human monocytic cell line (U937) were obtained from the Korean Cell Line Bank (KCLB, Korea). Dulbecco's modified Eagle's medium (DMEM), Minimum Essential Medium (MEM), McCoy's 5A Medium, Roswell Park Memorial Institute 1640 medium (RPMI-1640), fetal bovine serum (FBS), and penicillin–streptomycin solution (PS) were purchased from Welgene (Korea). Trypsin–EDTA solution was obtained from Zen-Bio (USA), and all cell culture plastics, including flasks, plates, Petri dishes, and confocal dishes, were sourced from SPL Life Science (Korea). Alginic acid sodium salt (alginate), calcium chloride ($CaCl_2$), dimethyl sulfoxide (DMSO), ethylenediaminetetraacetic acid (EDTA), trichloro(1*H*,1*H*,2*H*,2*H*-perfluorooctyl)silane, trypan blue solution, phorbol 12-myristate 13-acetate (PMA), lipopolysaccharide (LPS), nintedanib, gentamicin, polyethylene glycol diacrylate (PEGDA, MW 700 Da), polyethylene glycol (PEG, MW 600 Da), 2-hydroxy-2-methylpropiophenone (Darocur 1173), Tween 20, hydrogen peroxide solution (30% w/w), and biotinyl tyramide were obtained from Sigma-Aldrich (USA). Interferon gamma (IFN-γ), interleukin-4 (IL-4), interleukin-13 (IL-13), monoclonal antibodies targeting CD68, CD80, and CD206, tris(2-carboxyethyl) phosphine (TCEP), and streptavidin-phycoerythrin (SA-PE) were acquired from Thermo Fisher Scientific (USA). DUP, STX, TCZ, and TRA were purchased from MedChem Express (USA). Sodium citrate tribasic dihydrate was obtained from DukSan Reagent (Korea), and agarose was sourced from GeneOn (Germany). Alexa Fluor 488 anticollagen-I antibody and Alexa Fluor 647 antialpha smooth muscle actin antibody were purchased from Abcam (UK). Alexa Fluor 488 antiextra domain A fibronectin (IST-9) antibody was purchased from Santa Cruz Biotechnology (USA). Multiscreen 96-well plates (MSBVN1250) were obtained from Merck Millipore (USA). Enzyme-linked immunosorbent assay (ELISA) kits for IL-4, IL-6, and IL-13 were sourced from BT LAB (China), while the transforming growth factor-beta (TGF-β) ELISA kit and bovine serum albumin (BSA) were obtained from R&D Systems (USA). 4′,6-Diamidino-2-phenylindole (DAPI) was purchased from Sigma-Aldrich (USA). SU-8 100 photoresist was purchased from Kayaku Advanced Materials (USA), and 4-in. silicon wafers were obtained from WaferShop (Korea). Polydimethylsiloxane elastomer (SYLGARD 184 PDMS elastomer, base and curing agent) was sourced from Dow Corning (USA). Ethyl alcohol (ethanol), SU-8 developer (1-methoxy-2-propanol acetate), and isopropyl alcohol (IPA) were purchased from Samchun Pure Chemical (Korea) and Dae Myung Chemical (Korea). Phosphate buffered saline (PBS) tablets were obtained from Takara Korea Biomedical (Korea).

Encoded Hydrogel Microparticle Synthesis and Capture Antibody Functionalization. Encoded hydrogel microparticles (MPs) were synthesized using a discontinuous dewetting technique in a degassed micromold.[30] The synthesized MPs were functionalized via a thiol–ene click reaction, in which the thiol groups of the reduced antibody reacted with acrylate groups on the hydrogel surface.[44] For capture antibody reduction, reconstituted capture antibody (5 μL, 2 μg μL^{-1}) for IL-4, IL-6, IL-13, and TGF-β was incubated with TCEP (5 μL, 0.2 mm) at room temperature for 1 h. The reduced antibody solution (10 μL) was subsequently mixed with particle suspension (10 μL), and incubated at 25 °C for 48 h in a thermoshaker (MSC-100, Hangzhou Allsheng Instruments, China) at 1500 rpm. Following incubation, the particles were washed seven times with PBST (1× PBS containing 0.05% (v/v) Tween 20) and stored at 4 °C in PBST until further use.

Multiplex Immunoassay. Multiplex immunoassays were performed as previously described, with slight modifications.[31,32,44] Briefly, approximately 200 MPs per target, conjugated with capture antibodies for IL-4, IL-6, IL-13, and TGF-β, were incubated with target protein solution (2× in PBST) at 25 °C for 2 h with shaking at 1500 rpm in a 96-well filter plate. Following incubation, the wells were washed three times with PBST to retain only the hydrogel particles. The particles were then sequentially incubated with biotinylated detection antibodies (0.025 μg/μL) for 1 h, followed by SA-PE solution (0.02 mg/mL) for 30 min, both at 25 °C with shaking at 1500 rpm. After multiple PBST washes, the particles were resuspended in PBST (100 μL) for analysis.

Imaging. Brightfield and fluorescence imaging was performed as previously described. Briefly, particle suspension (10 μL) was placed onto a glass slide, and images were acquired using a Zeiss Axiovert 200 microscope. Fluorescence imaging was conducted using a LQ-HXP 120 fluorescence light source (Zeiss, Germany) with an excitation/emission filter set at λex/λem = 540/605 nm. The fluorescence exposure time was set to 70 ms, and final images were acquired in TIFF format. Image processing and fluorescence intensity quantification were performed using ImageJ software (National Institutes of Health, USA).

Cell Culture and Maintenance. Cell lines were maintained at 37 °C in a humidified atmosphere with 5% CO_2 and passaged upon reaching 70–80% confluence. U937 cells were cultured in RPMI-1640 medium supplemented with 10% FBS, while MRC-5 cells were maintained in MEM with HEPES (25 mm) and 10% FBS. Calu-1 cells were cultured in McCoy's 5A medium supplemented with 10% FBS. For subculturing, cells were enzymatically detached using trypsin–EDTA solution (1 mL), neutralized with an equivalent volume of fresh medium, and collected by centrifugation. The supernatant was removed, and the cell pellet was resuspended in fresh culture medium before incubation under standard culture conditions.

Macrophage Differentiation and Polarization. Macrophage differentiation and polarization were performed following previously

https://doi.org/10.1021/acsnano.5c08033
ACS Nano 2025, 19, 32361–32373

established protocols.[27,28] Briefly, U937 monocytes were first differentiated into M0 macrophages in standard culture plates using PMA (100 nm), followed by polarization into M1 and M2 macrophages via LPS (100 ng/mL)/IFN-γ (20 ng/mL) and IL-4 (20 ng/mL)/IL-13 (20 ng/mL)treatments, respectively. To ensure accurate cytokine quantification, differentiated macrophages were thoroughly washed with fresh medium to remove any residual differentiation agents, then harvested and seeded onto transwell inserts. The expression of CD68 (M0), CD80 (M1), and CD206 (M2) was evaluated using confocal laser scanning microscopy (CLSM).[45] Cells were fixed, permeabilized, and blocked under standard conditions, incubated overnight at 4 °C with primary antibodies, and subsequently stained with fluorescent secondary antibodies and DAPI. Fluorescence images were acquired using CLSM to confirm marker expression.

Alginate Microwell Preparation. Alginate microwells were fabricated via soft lithography using positive-patterned PDMS micromold, following a previously described method.[20] To generate microwells, 4% (w/v) sodium alginate in culture medium and 5% (w/v) agarose containing $CaCl_2$ (100 mm) in deionized water were prepared as previously reported, with minor modifications. Specifically, alginate solution (150 μL) was deposited onto O_2 plasma-treated micromolds, followed by ionic cross-linking with an agarose slab for 15 min. The cross-linked alginate microwells were peeled off and positioned at the bottom of a well plate. To prevent bacterial contamination, microwells were treated with gentamicin (10 μg/mL in MEM) and stored overnight in an incubator before use.

Formation and Harvesting of Coculture Spheroids. Alginate microwells prepared in 24-well plates were seeded with Calu-1 and MRC-5 cells (15×10^5 cells). To establish cocultures with macrophages, cell culture inserts containing macrophages were introduced into the wells (5×10^5 cells).[46] Spheroids were cultured for 48 h, with diameter and morphology monitored every 24 h using a brightfield microscope (Axiovert 200, Zeiss, Germany). For spheroid harvesting, the culture medium was removed, and wells were washed twice with PBS. To dissolve the alginate microwells, DMEM containing sodium citrate (10 mm) and EDTA (7 mm) was added. The spheroids were immediately collected, centrifuged to remove the supernatant, and resuspended in PBS for subsequent use.

Spheroid Cell Viability. Spheroid cell viability was assessed using the CellTiter-Glo 3D kit (Promega, USA) according to the manufacturer's instructions. Luminescence was measured using a microplate reader (SpectraMax iD5, Molecular Devices, USA). Proliferation was evaluated at 24 h intervals up to Day 2 of cultivation. An equal volume of CellTiter-Glo 3D reagent (1:1, v/v relative to the medium volume in each well) was added. The plate was incubated at room temperature for 25 min to stabilize the luminescent signal. Luminescence was then recorded using the same microplate reader.

Measurement of Mechanical Properties of Spheroids. Microfluidic channels were fabricated using photolithography and soft lithography techniques. Spheroids were introduced into the inlet of the microfluidic chip via a tygon tube, with flow controlled by a syringe pump. The mechanical properties of 3D spheroids were assessed by evaluating their deformability upon collision with a junction wall within a microfluidic chip, following a previously established method.[20] Deformability was measured at a fixed 48 h drug-exposure end point to enable standardized comparisons across conditions; the selection and optimization of this end point are described in Figure S16. Deformation events were recorded with a high-speed camera, and images were analyzed in Phantom Camera Control (PCC) and further processed in ImageJ software.

Pharmacological Treatment. For pharmacological experiments, MEM supplemented with 10% FBS was used as the base medium, serving as the negative control. The antifibrosis drug (NTD)[40] and interleukin-targeting drugs (DUP, TRA, TCZ, STX)[47−51] were added to the culture medium at a final concentration of 5 μg/mL. To assess their antifibrotic efficacy, drug solutions were introduced at the time of initial seeding, when epithelial cells, fibroblasts, and macrophages were cocultured to establish a fibrosis model. The fibrosis-induced coculture spheroids were harvested on day 2 of culture for further analysis.[52]

Immunostaining of Spheroids. Immunofluorescence staining was performed following a previously established protocol.[20] Briefly, fibrosis-induced coculture spheroids were fixed, permeabilized, and blocked under standard conditions, then incubated overnight at 4 °C with primary antibodies targeting collagen-I (Alexa Fluor 488, 1:100), IST-9 (Alexa Fluor 488, 1:100) and α-SMA (Alexa Fluor 647, 1:200). Nuclei were counterstained with DAPI (300 nm), and all washing steps were performed using PBS-T. Fluorescence images were acquired using a confocal laser scanning microscope (LSM700, Zeiss) under consistent imaging parameters. Image processing and fluorescence intensity quantification were conducted using ImageJ software. Fluorescence intensities were normalized by calculating the ratio of signal intensity within each spheroid to the corresponding DAPI-stained nuclear distribution area, ensuring a standardized comparison across samples.

qPCR Analysis. Total RNA was extracted from spheroid cocultures using TRIzol in combination with the AccuPrep Universal RNA Extraction Kit (AccuPrep, Bioneer), according to the manufacturer's instructions. RNA purity and concentration were evaluated using a NanoDrop 2000 spectrophotometer (NanoDrop 2000, Thermo Fisher Scientific), and integrity was confirmed with a 5200 Fragment Analyzer (5200 Fragment Analyzer, Agilent Technologies). cDNA was synthesized from total RNA using the AccuPower RocketScript Cycle RT PreMix (AccuPower RocketScript Cycle RT PreMix, Bioneer) on an AllInOneCycler PCR system (AllInOneCycler, Bioneer). Quantitative PCR was performed with the Exicycler 96 Real-Time Quantitative Thermal Block (Exicycler 96, Bioneer) using the AccuPower 2X GreenStar Master Mix (AccuPower 2X GreenStar Master Mix, Bioneer) and gene-specific primers (Table S3). Relative gene expression was calculated using the $2^{-\Delta\Delta C_T}$ method, with GAPDH serving as the reference gene.[53]

Statistical Analysis. All experiments were conducted in triplicate ($n = 3$) unless otherwise specified. Data are expressed as mean ± standard deviation (SD). Statistical significance between groups was assessed using a *t*-test, following an F-test for homogeneity of variances. If variances were equal, a student's *t*-test was applied; otherwise, a Welch's *t*-test was performed.

For multiple group comparisons, one-way ANOVA was conducted, followed by Tukey's post hoc test. Statistical significance was defined as $^*p < 0.05$, $^{**}p < 0.01$, $^{***}p < 0.001$, n.s.: not significant.

ASSOCIATED CONTENT

Supporting Information

The Supporting Information is available free of charge at https://pubs.acs.org/doi/10.1021/acsnano.5c08033.

Microfluidic collision video—control spheroid (Lung spheroid only) (MP4)

Microfluidic collision video—M0 macrophage co-culture spheroid (MP4)

Microfluidic collision video—M1 macrophage co-culture spheroid (MP4)

Microfluidic collision video—M2 macrophage co-culture spheroid (MP4)

Microfluidic collision video—M1/M2 co-culture spheroid (ratio 1:2.5) (MP4)

Microfluidic collision video—NTD-treated spheroid (MP4)

Microfluidic collision video—TCZ-treated spheroid (MP4)

Microfluidic collision video—STX-treated spheroid (MP4)

Microfluidic collision video—DUP-treated spheroid (MP4)

Microfluidic collision video—TRA-treated spheroid (MP4)

https://doi.org/10.1021/acsnano.5c08033
ACS Nano 2025, 19, 32361−32373

Determination of optimal macrophage polarization ratio (M1/M2); cytokine levels and fold changes in IPF patient samples compared to healthy controls, based on reported literature data; optimization of M1/M2 macrophage coculture ratio; differentiation and characterization of macrophage subtypes; confirmation of monocyte to macrophage differentiation and polarization; schematics and procedures of encoded hydrogel microparticle synthesis and multiplex cytokine immunoassay; standard curves for cytokine quantification; formation and characterization of uniformly sized macrophage coculture spheroids; cytokine secretion profiles and mechanical property evaluation after TGF-β treatment; spheroid deformability measurement using a microfluidic device; immunofluorescence analysis of α-SMA expression costained with collagen-I or EDA-FN; schematic representation of therapeutic mechanisms of anti-interleukin drug action in fibrosis (Tables S1−S3, Figures S1−S16) (PDF)

AUTHOR INFORMATION

Corresponding Author

Ki Wan Bong − *Department of Chemical and Biological Engineering, Korea University, Seoul 02841, Republic of Korea*; orcid.org/0000-0001-5026-0757; Email: bong98@korea.ac.kr

Authors

Bolam Kim − *Department of Chemical and Biological Engineering, Korea University, Seoul 02841, Republic of Korea*

Hye Won Kim − *Department of Chemical and Biological Engineering, Korea University, Seoul 02841, Republic of Korea*

Jeong Yeon Kim − *Department of Chemical and Biological Engineering, Korea University, Seoul 02841, Republic of Korea*

In Yeong Cho − *Department of Chemical and Biological Engineering, Korea University, Seoul 02841, Republic of Korea*

Wookyoung Jang − *Department of Chemical and Biological Engineering, Korea University, Seoul 02841, Republic of Korea*

Hyunsik Choi − *Department of Materials Science and Engineering, Pohang University of Science and Technology (POSTECH), Pohang, Gyeongbuk 37673, Republic of Korea*

Complete contact information is available at: https://pubs.acs.org/10.1021/acsnano.5c08033

Author Contributions

[§]B.K. and H.W.K. contributed equally to this work.

Funding

National of Research Foundation of Korea, Ministry of Science and ICT (MSIT). Grant Numbers: RS-2023-00253210, RS-2024-00456113, and RS-2025-02263336. National of Research Foundation of Korea, Ministry of Education. Grant Numbers: RS-2022-NR075543 and RS-2024-00460035

Notes

The authors declare no competing financial interest.

ACKNOWLEDGMENTS

This work was supported by Basic Science Research Program through the National Research Foundation of Korea (NRF) grant funded by the Korea government, Ministry of Science and ICT (MSIT) (RS-2023-00253210, RS-2024-00456113, RS-2025-02263336) and the Ministry of Education (RS-2022-NR075542, RS-2024-00460035).

REFERENCES

(1) Lederer, D. J.; Martinez, F. J. Idiopathic Pulmonary Fibrosis. *N. Engl. J. Med.* **2018**, *378*, 1811−1823.

(2) Bitterman, P. B.; Wewers, M. D.; Rennard, S. I.; Adelberg, S.; Crystal, R. G. Modulation of Alveolar Macrophage-Driven Fibroblast Proliferation by Alternative Macrophage Mediators. *J. Clin. Invest.* **1986**, *77*, 700−708.

(3) Zhou, Y.; Peng, H.; Sun, H.; Peng, X.; Tang, C.; Gan, Y.; Chen, X.; Mathur, A.; Hu, B.; Slade, M. D.; et al. Chitinase 3-like 1 Suppresses Injury and Promotes Fibroproliferative Responses in Mammalian Lung Fibrosis. *Sci. Transl. Med.* **2014**, *6*, 240ra276.

(4) Misharin, A. V.; Morales-Nebreda, L.; Reyfman, P. A.; Cuda, C. M.; Walter, J. M.; McQuattie-Pimentel, A. C.; Chen, C. I.; Anekalla, K. R.; Joshi, N.; Williams, K. J. N.; et al. Monocyte-Derived Alveolar Macrophages Drive Lung Fibrosis and Persist in the Lung over the Life Span. *J. Exp. Med.* **2017**, *214*, 2387−2404.

(5) Kamiya, M.; Carter, H.; Espindola, M. S.; Doyle, T. J.; Lee, J. S.; Merriam, L. T.; Zhang, F.; Kawano-Dourado, L.; Sparks, J. A.; Hogaboam, C. M.; et al. Immune Mechanisms in Fibrotic Interstitial Lung Disease. *Cell* **2024**, *187*, 3506−3530.

(6) Pokhreal, D.; Crestani, B.; Helou, D. G. Macrophage Implication in IPF: Updates on Immune, Epigenetic, and Metabolic Pathways. *Cells* **2023**, *12*, 2193.

(7) Inomata, M.; Nishioka, Y.; Azuma, A. Nintedanib: Evidence for Its Therapeutic Potential in Idiopathic Pulmonary Fibrosis. *Core Evidence* **2015**, *10*, 89−98.

(8) Raghu, G.; Selman, M. Nintedanib and Pirfenidone: New Antifibrotic Treatments Indicated for Idiopathic Pulmonary Fibrosis Offer Hopes and Raises Questions. *Am. J. Respir. Crit. Care Med.* **2015**, *191*, 252−254.

(9) Lin, X.; Wen, J.; Liu, R.; Gao, W.; Qu, B.; Yu, M. Nintedanib Inhibits TGF-β-Induced Myofibroblast Transdifferentiation in Human Tenon's Fibroblasts. *Mol. Vision* **2018**, *24*, 789−800.

(10) Ma, J.; Li, G.; Wang, H.; Mo, C. Comprehensive Review of Potential Drugs with Anti-Pulmonary Fibrosis Properties. *Biomed. Pharmacother.* **2024**, *173*, 116282.

(11) Raghu, G.; Remy-Jardin, M.; Richeldi, L.; Thomson, C. C.; Inoue, Y.; Johkoh, T.; Kreuter, M.; Lynch, D. A.; Maher, T. M.; Martinez, F. J.; et al. Idiopathic Pulmonary Fibrosis (an Update) and Progressive Pulmonary Fibrosis in Adults: An Official ATS/ERS/JRS/ALAT Clinical Practice Guideline. *Am. J. Respir. Crit. Care Med.* **2022**, *205*, e18−e47.

(12) Murray, L. A.; Zhang, H.; Oak, S. R.; Coelho, A. L.; Herath, A.; Flaherty, K. R.; Lee, J.; Bell, M.; Knight, D. A.; Martinez, F. J.; et al. Targeting Interleukin-13 with Tralokinumab Attenuates Lung Fibrosis and Epithelial Damage in a Humanized SCID Idiopathic Pulmonary Fibrosis Model. *Am. J. Respir. Cell Mol. Biol.* **2014**, *50*, 985−994.

(13) Parker, J. M.; Glaspole, I. N.; Lancaster, L. H.; Haddad, T. J.; She, D.; Roseti, S. L.; Fiening, J. P.; Grant, E. P.; Kell, C. M.; Flaherty, K. R. A Phase 2 Randomized Controlled Study of Tralokinumab in Subjects with Idiopathic Pulmonary Fibrosis. *Am. J. Respir. Crit. Care Med.* **2018**, *197*, 94−103.

(14) Brown, A. C.; Fiore, V. F.; Sulchek, T. A.; Barker, T. H. Physical and Chemical Microenvironmental Cues Orthogonally Control the Degree and Duration of Fibrosis-Associated Epithelial-to-Mesenchymal Transitions. *J. Pathol.* **2013**, *229*, 25−35.

(15) Cross, S. E.; Jin, Y.-S.; Tondre, J.; Wong, R.; Rao, J.; Gimzewski, J. K. AFM-Based Analysis of Human Metastatic Cancer Cells. *Nanotechnology* **2008**, *19*, 384003.

(16) Faria, E. C.; Ma, N.; Gazi, E.; Gardner, P.; Brown, M.; Clarke, N. W.; Snook, R. D. Measurement of Elastic Properties of Prostate Cancer Cells Using AFM. *Analyst* **2008**, *133*, 1498−1500.

(17) Jaiswal, D.; Cowley, N.; Bian, Z.; Zheng, G.; Claffey, K. P.; Hoshino, K. Stiffness Analysis of 3D Spheroids Using Microtweezers. *PLoS One* **2017**, *12*, No. e0188346.

(18) Tomizawa, Y.; Wali, K. H.; Surti, M.; Suhail, Y.; Kshitiz; Hoshino, K. Single-Cell Quantification of Viscoelastic Phase Transitions in 3D Tissues. *Adv. Mater. Technol.* **2025**, *10*, 2401302.

(19) Boot, R. C.; van der Net, A.; Gogou, C.; Mehta, P.; Meijer, D. H.; Koenderink, G. H.; Boukany, P. E. Cell Spheroid Viscoelasticity Is Deformation-Dependent. *Sci. Rep.* **2024**, *14*, 20013.
(20) Kim, B.; Kim, J. Y.; Kim, H. W.; Cho, I. Y.; Bong, K. W. Fibrosis Drug Efficacy Assessment Based on Microfluidic Mechanical Property Evaluation of Spheroid Models. *Adv. Healthcare Mater.* **2025**, *14*, No. e2403842.
(21) Gao, X.; Jia, G.; Guttman, A.; DePianto, D. J.; Morshead, K. B.; Sun, K. H.; Ramamoorthi, N.; Vander Heiden, J. A.; Modrusan, Z.; Wolters, P. J.; et al. Osteopontin Links Myeloid Activation and Disease Progression in Systemic Sclerosis. *Cell Rep. Med.* **2020**, *1*, 100140.
(22) Kuznetsova, A. B.; Kolesova, E. P.; Parodi, A.; Zamyatnin, A. A.; Egorova, V. S. Reprogramming Tumor-Associated Macrophage Using Nanocarriers: New Perspectives to Halt Cancer Progression. *Pharmaceutics* **2024**, *16*, 636.
(23) Zhang, C.; Yang, M.; Ericsson, A. C. Function of Macrophages in Disease: Current Understanding on Molecular Mechanisms. *Front. Immunol.* **2021**, *12*, 620510.
(24) Yang, G.; Yang, Y.; Liu, Y.; Liu, X. Regulation of Alveolar Macrophage Death in Pulmonary Fibrosis: A Review. *Apoptosis* **2023**, *28*, 1505−1519.
(25) Witherel, C. E.; Abebayehu, D.; Barker, T. H.; Spiller, K. L. Macrophage and Fibroblast Interactions in Biomaterial-Mediated Fibrosis. *Adv. Healthcare Mater.* **2019**, *8*, No. e1801451.
(26) Cai, Y.; Sugimoto, C.; Arainga, M.; Alvarez, X.; Didier, E. S.; Kuroda, M. J. In Vivo Characterization of Alveolar and Interstitial Lung Macrophages in Rhesus Macaques: Implications for Understanding Lung Disease in Humans. *J. Immunol.* **2014**, *192*, 2821−2829.
(27) Song, M. G.; Ryoo, I. G.; Choi, H. Y.; Choi, B. H.; Kim, S. T.; Heo, T. H.; Lee, J. Y.; Park, P. H.; Kwak, M. K. NRF2 Signaling Negatively Regulates Phorbol-12-Myristate-13-Acetate (PMA)-Induced Differentiation of Human Monocytic U937 Cells into Pro-Inflammatory Macrophages. *PLoS One* **2015**, *10*, No. e0134235.
(28) Nascimento, C. R.; Rodrigues Fernandes, N. A.; Gonzalez Maldonado, L. A.; Rossa Junior, C. Comparison of Monocytic Cell Lines U937 and THP-1 as Macrophage Models for in vitro Studies. *Biochem. Biophys. Rep.* **2022**, *32*, 101383.
(29) Jang, W.; Song, E. L.; Mun, S. J.; Bong, K. W. Efficient Isolation of Encoded Microparticles in a Degassed Micromold for Highly Sensitive and Multiplex Immunoassay with Signal Amplification. *Biosens. Bioelectron.* **2024**, *261*, 116465.
(30) Jang, W.; Mun, S. J.; Kim, S.-Y.; Bong, K. W. Controlled Growth Factor Delivery via a Degradable Poly(lactic acid) Hydrogel Microcarrier Synthesized Using Degassed Micromolding Lithography. *Colloids Surf., B* **2023**, *222*, 113088.
(31) Choi, J. H.; Jang, W.; Lim, Y. J.; Mun, S. J.; Bong, K. W. Highly Flexible Deep-Learning-Based Automatic Analysis for Graphically Encoded Hydrogel Microparticles. *ACS Sens.* **2023**, *8*, 3158−3166.
(32) Mun, S. J.; Jang, W.; Park, H.-S.; Lim, Y. J.; Yang, T.-J.; Bong, K. W. Multiplex Genotyping of SNPs in Genomic DNA via Hydrogel-Based Assay Mediated with MutS and Polyethylene Glycol. *Biosens. Bioelectron.* **2023**, *241*, 115670.
(33) Truong Hoang, Q.; Kim, D. Y.; Park, H. S.; Jang, W.; Nguyen Cao, T. G.; Kang, J. H.; Ko, Y. T.; Mun, S. J.; Bhang, S. H.; Shim, M. S.; et al. Oxygen-Supplying Piezocatalytic Therapy of Hypoxic Tumors by Intratumoral Delivery of pH-Responsive Multicompartmental Carriers with Sequential Drug Release Capability. *Adv. Funct. Mater.* **2024**, *34*, 2306078.
(34) Sharifiaghdam, M.; Shaabani, E.; Faridi-Majidi, R.; De Smedt, S. C.; Braeckmans, K.; Fraire, J. C. Macrophages as a Therapeutic Target to Promote Diabetic Wound Healing. *Mol. Ther.* **2022**, *30*, 2891−2908.
(35) Jiang, H.; Weng, X.; Li, D. A Novel Microfluidic Flow Focusing Method. *Biomicrofluidics* **2014**, *8*, 054120.
(36) Bonifazi, M.; Di Vincenzo, M.; Caffarini, M.; Mei, F.; Salati, M.; Zuccatosta, L.; Refai, M.; Mattioli-Belmonte, M.; Gasparini, S.; Orciani, M. How the Pathological Microenvironment Affects the Behavior of Mesenchymal Stem Cells in the Idiopathic Pulmonary Fibrosis. *Int. J. Mol. Sci.* **2020**, *21*, 8140.
(37) Park, S. W.; Ahn, M. H.; Jang, H. K.; Jang, A. S.; Kim, D. J.; Koh, E. S.; Park, J. S.; Uh, S. T.; Kim, Y. H.; Park, J. S.; et al. Interleukin-13 and Its Receptors in Idiopathic Interstitial Pneumonia: Clinical Implications for Lung Function. *J. Korean Med. Sci.* **2009**, *24*, 614−620.
(38) Martinez-Nunez, R. T.; Louafi, F.; Sanchez-Elsner, T. The Interleukin 13 (IL-13) Pathway in Human Macrophages Is Modulated by microRNA-155 via Direct Targeting of Interleukin 13 Receptor Alpha1 (IL13Ralpha1). *J. Biol. Chem.* **2011**, *286*, 1786−1794.
(39) She, Y. X.; Yu, Q. Y.; Tang, X. X. Role of Interleukins in the Pathogenesis of Pulmonary Fibrosis. *Cell Death Discovery* **2021**, *7*, 52.
(40) Hostettler, K. E.; Zhong, J.; Papakonstantinou, E.; Karakiulakis, G.; Tamm, M.; Seidel, P.; Sun, Q.; Mandal, J.; Lardinois, D.; Lambers, C.; et al. Anti-Fibrotic Effects of Nintedanib in Lung Fibroblasts Derived from Patients with Idiopathic Pulmonary Fibrosis. *Respir. Res.* **2014**, *15*, 157.
(41) Nishimoto, N.; Kishimoto, T. Interleukin 6: From Bench to Bedside. *Nat. Clin. Pract. Rheumatol.* **2006**, *2*, 619−626.
(42) Alraouji, N. N.; Aboussekhra, A. Tocilizumab Inhibits IL-8 and the Proangiogenic Potential of Triple Negative Breast Cancer Cells. *Mol. Carcinog.* **2021**, *60*, 51−59.
(43) Khanna, D.; Lin, C. J. F.; Furst, D. E.; Wagner, B.; Zucchetto, M.; Raghu, G.; Martinez, F. J.; Goldin, J.; Siegel, J.; Denton, C. P. Long-Term Safety and Efficacy of Tocilizumab in Early Systemic Sclerosis-Interstitial Lung Disease: Open-Label Extension of a Phase 3 Randomized Controlled Trial. *Am. J. Respir. Crit. Care Med.* **2022**, *205*, 674−684.
(44) Lee, H. J.; Kim, J. Y.; Roh, Y. H.; Kim, S. M.; Bong, K. W. Linker-Free Antibody Conjugation for Sensitive Hydrogel Microparticle-Based Multiplex Immunoassay. *Analyst* **2019**, *144*, 6712−6720.
(45) Chong, L.; Jiang, Y.-W.; Wang, D.; Chang, P.; Xu, K.; Li, J. Targeting and Repolarizing M2-Like Tumor-Associated Macrophage-Mediated MR Imaging and Tumor Immunotherapy by Biomimetic Nanoparticles. *J. Nanobiotechnol.* **2023**, *21*, 401.
(46) Tajima, T.; Murata, T.; Aritake, K.; Urade, Y.; Hirai, H.; Nakamura, M.; Ozaki, H.; Hori, M. Lipopolysaccharide Induces Macrophage Migration via Prostaglandin D(2) and Prostaglandin E(2). *J. Pharmacol. Exp. Ther.* **2008**, *326*, 493−501.
(47) Kwon, B. J.; Cho, N. H.; Ahn, T.; Kim, G.; Diệu, N. T. X.; Kim, W. T.; Cho, H.-J.; Seo, D. H.; Kim, J. Y. Nicotiana Benthamiana-Derived Dupilumab-scFv Reaches Deep into the Cultured Human Nasal Epithelial Cells and Inhibits CCL26 Expression. *Sci. Rep.* **2024**, *14*, 14558.
(48) Zhang, L.; Ding, Y.; Wang, Q.; Pan, W.; Wei, Z.; Smith, P. A.; Yang, X. Preclinical Immunological Characterization of Rademikibart (CBP-201), a Next-Generation Human Monoclonal Antibody Targeting IL-4Rα, for the Treatment of Th2 Inflammatory Diseases. *Sci. Rep.* **2023**, *13*, 12411.
(49) Tollenaere, M. A. X.; Mølck, C.; Henderson, I.; Pollack, S.; Addis, P.; Petersen, H. H.; Norsgaard, H. Tralokinumab Effectively Disrupts the IL-13/IL-13Rα1/IL-4Rα Signaling Complex but Not the IL-13/IL-13Rα2 Complex. *JID Innovations* **2023**, *3*, 100214.
(50) Kittirat, Y.; Suksawat, M.; Thongchot, S.; Padthaisong, S.; Phetcharaburanin, J.; Wangwiwatsin, A.; Klanrit, P.; Sangkhamanon, S.; Titapun, A.; Loilome, W.; et al. Interleukin-6-Derived Cancer-Associated Fibroblasts Activate STAT3 Pathway Contributing to Gemcitabine Resistance in Cholangiocarcinoma. *Front. Pharmacol* **2022**, *13*, 897368.
(51) Coward, J.; Kulbe, H.; Chakravarty, P.; Leader, D.; Vassileva, V.; Leinster, D. A.; Thompson, R.; Schioppa, T.; Nemeth, J.; Vermeulen, J.; et al. Interleukin-6 as a Therapeutic Target in Human Ovarian Cancer. *Clin. Cancer Res.* **2011**, *17*, 6083−6096.
(52) Ham, I. H.; Oh, H. J.; Jin, H.; Bae, C. A.; Jeon, S. M.; Choi, K. S.; Son, S. Y.; Han, S. U.; Brekken, R. A.; Lee, D.; et al. Targeting Interleukin-6 as a Strategy to Overcome Stroma-Induced Resistance to Chemotherapy in Gastric Cancer. *Mol. Cancer* **2019**, *18*, 68.
(53) Lee, J.; Shin, H.; Seo, S.; Choi, J.; Kang, M.; Lee, Y.; Yi, M.; Gong, S. P.; Kang, H. W. Effect of Dual Optical Pulse Scheme with Supra and Subthreshold Fluences on Laser Micro Ablation of Pigment. *Sci. Rep.* **2025**, *15*, 24649.

https://doi.org/10.1021/acsnano.5c08033
ACS Nano 2025, 19, 32361−32373